Journal of Data Acquisition and Processing
ISSN: 1004-9037
https://sjcjycl.cn/
DOI: 10.5281/zenodo.7778311

MECHANICAL, OPTICAL, ELECTRONIC AND VIBRATIONAL PROPERTIES OF LIMNO4 AND LIMN2O4: DFT STUDY

R. Parvin[1], M. S. Ali[2]*
1Department of Physical Science, School of Engineering Sciences and Technology, Independent University Bangladesh.
[2]*Department of Physics, Faculty of Science, Pabna University of Science and Technology, Pabna-6600
*Corresponding Author: msali@pust.ac.bd
*Department of Physics, Faculty of Science, Pabna University of Science and Technology, Pabna-6600

Abstract
LiMn2O4 shows an overlap of electron path which reveals the metallic properties whereas for LiMnO4 there exists a band gap around 0.852 eV. From elastic tensor analysis anisotropic behavior is observed. But for LiMn2O4, Linear compressibility shows complete isotropic behavior. The contribution at the fermi level mainly comes from the O 2p and Mn 3d states. The electron- and hole-like sheets make the complex multi sheet. The highest reflectivity (~80%) was observed for LiMnO4 at ~ 17 eV in the IR-visible-UV region. The higher value of heat capacity for LiMnO4 indicates that it is softer compared to LiMn2O4.
Keywords: DFT simulation; Electronic and optical properties; Vibrational properties;

Introduction

At present, the demand for reliable energy and renewable energy storage is dramatically increasing due to fossil fuels and associated energy problems for environment. For a long period, Lithium-ion batteries are the most attractive energy sources for their superior energy density for electronic devices, especially for portable devices, for example, digital cameras, laptops and cell phones, and so on. The emerging new technologies broadly dependent on the development and application of lithium-ion batteries for the energy storage system to the next generation [1–4]. For transportation and smart grids renewable energy sources are very much important issues. For lithium-ion batteries, the lithium is transformed at the time of charge/discharge processes between electrodes. The lithium battery is consisting of a graphite with negative charged electrode, a liquid electrolyte, and a layered of LiCoO2, positive electrode. During this period of time, for charge compensation the electrons pass through the external circuit. In the case of commercial application of lithium-ion batteries, LiCoO2, LiFePO4, and LiMn2O4 are used as cathode materials whereas graphite is used as an anode material [5-8]. For the practical use of cathode materials, every procedure some its advantages and disadvantages. LiCoO2 as a cathode material has revolutionized for the use of portable electronic devices like laptops, phones, and so on. At the same time, the use of LiCoO2 is highly safe, low cost, and toxicity concern which is prevented from being used of LiCoO2 in broad-scale batteries and transportation systems to the next generation.

In recent years, though the development of LiFePO4 has been observed in safety issues, the high cost of carbon-coated nano-LiFePO4 limits its application for lithium-ion batteries [9, 10]. On the other hand, the LiMn2O4 has been attracted mostly as a cathode material for transportation and large-scale batteries due to its minimum cost, environmentally benign, excellent structural stability, and better -improved safety issues [11]. LiMn2O4 exists in the spinel structure with the space group of F-d 3m. For this material the Li and Mn occupy at the 8a tetrahedral and 16d octahedral sites whereas the oxygen ions of the cubic close-packed, respectively. Due to the edge-shared octahedral Mn2O4 host structure, this material is highly stable and possesses a very intersecting tunnels formed by the face-sharing of tetrahedral lithium (8a) sites and empty octahedral (16c) sites. This type of tunnel allows the three-dimensional diffusion of lithium ions for the charging and discharging process. In the case of lithium-ion batteries, it was found that by using LiMn2O4 as LiMn2O4/carbon as a cathode, the structural stability, rate of capacity, and cycling stability could improve. Up to date the different nanostructures of LiMn2O4 have been developed and applied as the cathode materials [12-22]. The above interesting properties motivated us to carry out further property calculations using the first-principles method.

In the present study, we have studied the different properties of LiMn2O4 and LiMnO4 by calculating minimum energy based on DFT implemented in the CASTEP code.

Research Methodology

The first-principles investigations have carried out by employing the plane-wave pseudo-potential approach with GGA developed by Perdew–Burke–Ernzerh within the DFT as implemented in the CASTEP code. Plane-wave cut-off energy will be employed throughout the calculations to determine the number of plane waves in expansion. The geometry optimizations will be performed using the BFGS minimization technique. To fulfill this purpose, successive geometry optimizations were performed with different cut-off energies, keeping k-points constant. Again, with different k-points keeping cut-off energy fixed at a particular k-mesh for LiMnO4 and LiMn2O4, respectively. We have used Monkhorst-Pack (MP) grid 9 x 6 x 8 and 9 x 9 x 9, to sample the Brillouin zone LiMnO4 and LiMn2O4 respectively. The cut-off energy was fitted with 500 eV for both cases. The quasi-harmonic Debye model implemented in the Gibbs program was employed to determine the thermodynamic properties at ambient conditions. In this investigation, we have used energy-volume data calculated from the third-order Birch–Murnaghan equation of state using the zero temperature and zero pressure equilibrium values of energy, volume, and bulk modulus evaluated from the present DFT calculations [23-35].

Structural Properties

Table 1. Calculated and available theoretical and experimental lattice parameters a, b, and c (Å) and unit cell volume Vo (Å3) at zero pressure for LiMn2O4 and LiMnO4.

Compound	*a*	*b*	*c*o	*V*o	*Ref.*
LiMnO4	5.0861	8.5032	6.563	294.453	This
	$5.514^{Ex.}$	8.397	6.359	-----	[36]

	5.54Theo.	8.50	6.58	310.25	[37]
	8.824Ex.	-	-	-	[38]
LiMn2O4	8.242Ex.	-	-	-	[39]
	8.662			459.662	This

The calculated values of fully relaxed equilibrium structural parameters of these phases are presented in Table 1, along with the available experimental values and other theoretical results. The comparison shows that our calculated results are in excellent agreement with both the theoretical and experimental values. Fig.1 shows the crystal structure of our studied compound LiMnO4 and LiMn2O4, respectively.

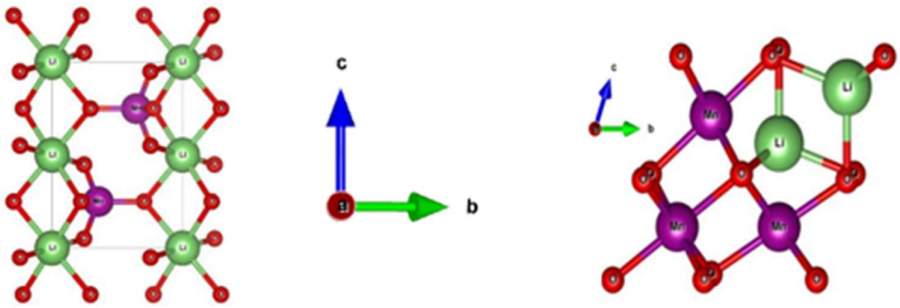

Fig. 1: Standard View of Crystal Structure of 2-Dimensional LiMnO4 and LiM2nO4.

In the case of LiMnO4 the crystal structure (space group: Cmcm) is an orthorhombic structure with the position 4a, 4c, 8f and 8g for Li, Mn, and O, respectively. The spinel structure of LiMn2O4, (space-group: Fd-3m), Li in the 8 a site, Mn ions are located in the 16 d site, a cubic close-packed (ccp) array of oxygen ions occupies the 32 e position. The Mn ions with the oxygens have octahedral coordination, and the MnO6 octahedra share edges in a three-dimensional host for the Li guest ions. The 8 a tetrahedral site is situated furthest away from the 16 d site of all the interstitial tetrahedra (8 a, 8 b, and 48 f) and octahedra (16 c). The 8 a-tetrahedron faces are shared with an adjacent, vacant 16 c site. This structural features in the stoichiometric spinel compound executes a highly stable structure [36-42].

Mechanical Properties:

Elastic Constants, Cij and Mechanical Stability

Essentially, the elastic constants values of any solid allow us to obtain the mechanical stiffness properties and they can be used to delineate the resistance of any crystal to an applied stress. As a consequence of this, the mechanical behaviour as far as its elastic constants understanding are essential to investigate of LiMnO4 and LiMn2O4 compounds. The elastic stability conditions for each crystal system and Laue class, closed-form expressions can be found from the below given approaches. For this purpose, the matrix formulated into the block diagonal frame and the minors starting were expresses with the with the smallest blocks. Finally, we have checked the results presented below through direct calculation with computer simulations, the characteristic expanding in each case to the polynomial of the stiffness matrix, and factoring

it [43-46]. The calculated elastic constants of these compounds are presented in Table 2. The tabulated data in Table 2, all of the elastic constants for the compounds bear the stability criteria.

Table 2: Calculated elastic constants Cij (GPa) at 0 K temperature and 0 GPa pressure for LiMnO4 and LiMn2O4.

Compounds	C_{11}	C_{12}	C_{13}	C_{22}	C_{23}	C_{33}	C_{44}	C_{55}	C_{66}	*Ref.*
$LiMnO_4$	53	30	18	90	29	112	25	20	21	This
$LiMn_2O_4$	129	27	-	-	-	-	73	-	-	This

Elastic Tensor Analysis

Young's modulus, Y (u) is a measurement of the stiffness of a structure under the uniaxial strain to the unidirectional unit vector u. Shear modulus G (u, v) signifies the resistance to shear stress of the plane perpendicular to v in the direction of u, Poisson's ratio ν (u, v) is the ratio of transverse strain in the direction of v to the axial strain in the direction u under uniaxial deformation stage. The compression along a direction u upon isostatic compression express the Linear compressibility, K (= 1/B) (u) [47 - 50]. An absolute circle/sphere describe an isotropic solid and conversely. From the elastic moduli analysis, the anisotropy stage can be understood from the deviation of circular (for 2D) and spherical (for 3D) presentation.

Fig. 2 (a), in the case of xy plane the maximum value of Young's modulus is at the vertical axis whereas for the horizontal axis for all cases along xy, xz and yz axis there is a minimum value exists. The deviation along vertical axis is higher compared to the horizontal axis. The value reveals that all the planes are anisotropic. Fig. 4 (a) shows 3-D view of Young's modulus. Fig. 2. (b) shows the linear compressibility, K (1/B) of LiMnO4 for a 2-dimentional view whereas Fig. 4 (b), shows a 3-dimensional view. In the case of linear compressibility along xy and xz plane the behavior is almost the same. The deviation is minimum for the vertical axis whereas the deviation is maximum along the horizontal axis.

Fig. 3. (a) shows the shear modulus, G of LiMnO4 for the 2-dimentional view whereas fig. 4 (c) shows the 3-dimensional view. The value of the shear modulus is different for different plane. It is observed that the shear modulus shows anisotropic properties. Fig. 3. (b) shows the Poisson's ratio, υ of for the 2-dimentional view whereas fig. 4 (d) shows the 3-dimensional view. The value of Poisson's ratio is randomly changed in the horizontal and vertical axis. There exists a zigzag path. Hence, Poisson's ratio represents anisotropic properties [51, 52].

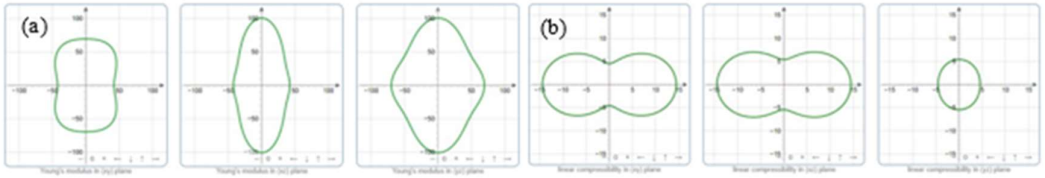

Fig. 2: The 2D plots of (a) Young's modulus, Y and (b) Linear compressibility, K for LiMnO4 compound, along xy, yz, and zx respectively.

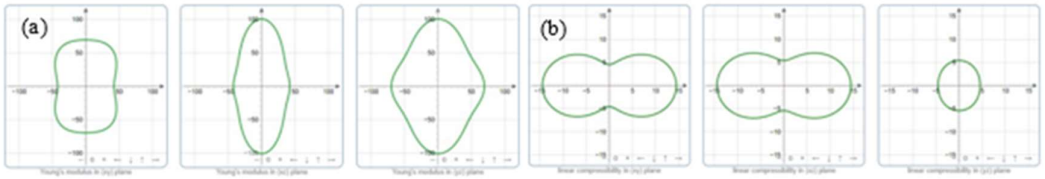

Fig. 3: The 2D plots of (a) Shear modulus, G, and (b) Poisson's ratio, υ for LiMnO4 compound along xy, yz, and zx respectively.

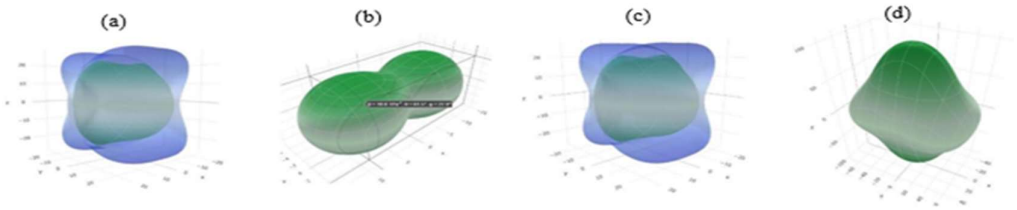

Fig. 4: The 3D plots of (a) Young's modulus, Y (b) Linear compressibility, K, (c) Shear modulus, G and, (d) Poisson's ratio, υ (right) for LiMnO4 compound.

Fig. 5 (a) shows Young's modulus of LiMn2O4 for a 2-dimentional view whereas Fig. 7 (a), shows a 3-dimensional view. It is observed that for xy, xz, and yz plane there exists deviation which shows anisotropic behavior. Fig. 5 (b) shows the linear compressibility, K (1/B) of LiMn2O4 for the 2-dimentional view whereas Fig. 7 (b), shows a 3-dimensional view. Along xy, xz, and xz plane the behavior is almost the same. There is no deviation for any axis along horizontal and vertical. Hence, the linear compressibility shows perfectly isotropic properties. Fig. 6 (a) shows shear modulus, G of LiMn2O4 for a 2-dimentional view whereas Fig. 7 (c) shows 3-dimensional view. Shear modulus for all the cases is deviated for different plane. Fig. 6 (b) shows the Poisson's ratio, υ of for a 2-dimentional view whereas Fig. 7 (d) shows a 3-dimensional view. The value of Poisson's ratio is a little-bit changed in in the xy, xz and yz plane in both the horizontal and vertical axis. Both are representing anisotropic properties [51 - 55].

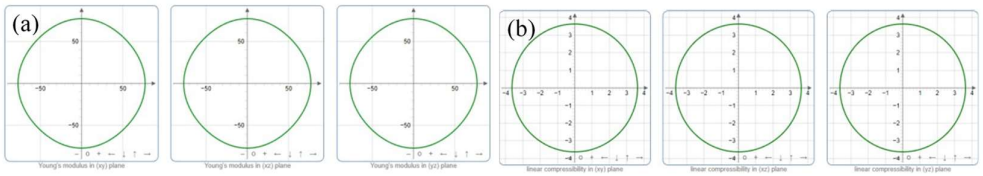

Fig. 5: The 2D plots of (a) Young's modulus, Y for LiMn2O4 and (b) Linear compressibility, K for LiMn2O4 compound, along xy, yz, and zx respectively

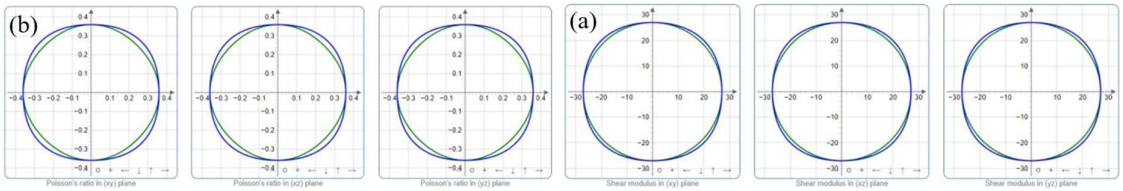

Fig. 6: The 2D plots of (a) Shear modulus, G for LiMn2O4 and (b) Poisson's ratio, υ for LiMn2O4 compound, along xy, yz, and zx respectively.

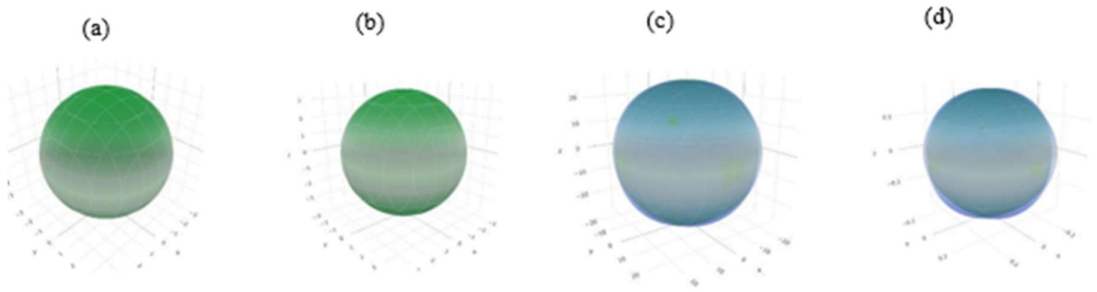

Fig. 7: The 3D plots of (a) Young's modulus, Y (b) Linear compressibility, K (c) Shear modulus, G and, (d) Poisson's ratio, υ (right) for LiMn2O4 compound.

Electronic Properties

Band Structure and Density of States (DOS)

The energy bands in the first Brillouin zone of the high symmetry directions are shown in the energy range from -5 to +4 eV for LiMnO4 whereas for LiMn2O4 the range was used -5 to +3 eV in Fig. 8 (a) and (b). At zero external pressure, the band gap of LiMnO4 was observed 0.852 eV. The previously reported band gap was 1.570 eV [37]. However, in the case of LiMn2O4, it was observed that the bands overlap each other. The number of sates of each energy level can be understand from the study of DOS in statistical and solid-state physics. Usually, a high DOS at a specific energy level measure that there are more available states for electrons [56]. Figure 9 express the TDOS of LiMnO4 and LiMn2O4, respectively. For both cases, we observe that the lowest energy bands lying between -7.0 eV and -2.0 eV arise mainly from the O 2p and Mn 3d states with a small contribution from Li 2s and O 2s, 2p, Mn 4s states. On the other hand, the energy bands from - 0.5 eV to the Fermi level are derived mainly from O 2p states with small contributions from Mn 4s and 4p 3p, with Li 2s states. Hence, we can say that, at the Fermi level, the main contribution to the total DOS comes from the O 2p and Mn 3d states respectively in both cases.

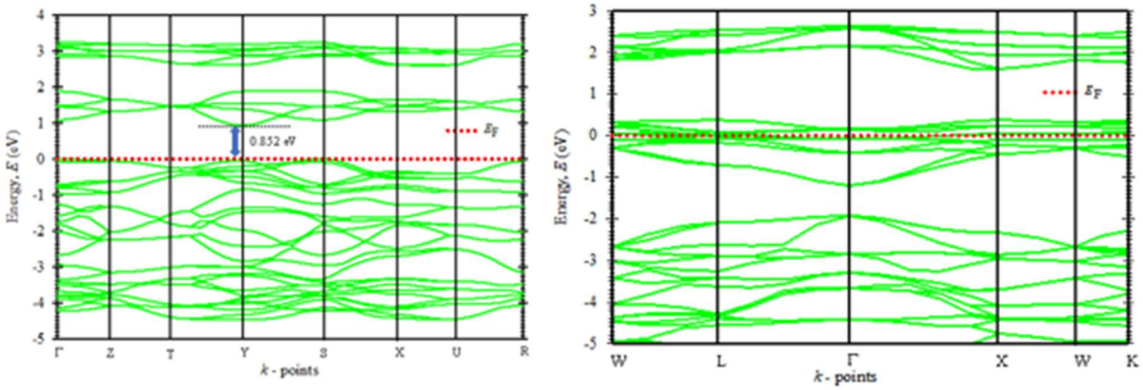

Fig. 8: Band structure of (a) LiMnO4 and (b) LiMn2O4.

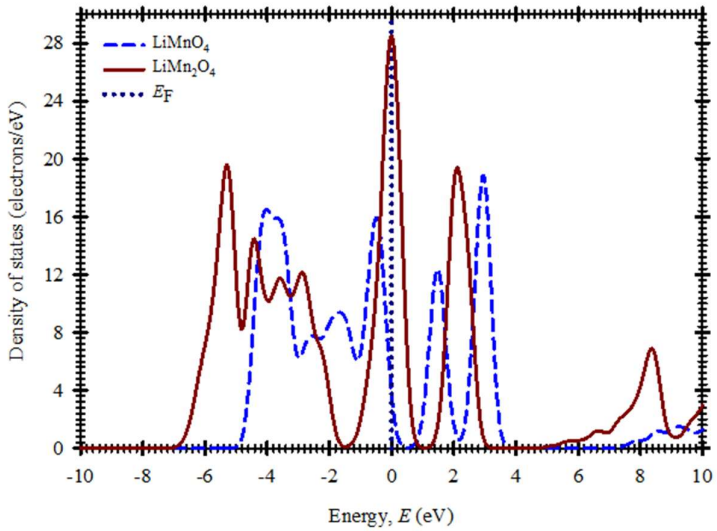

Fig. 9: Total density of states (DOS) of LiMnO4 and LiMn2O4.

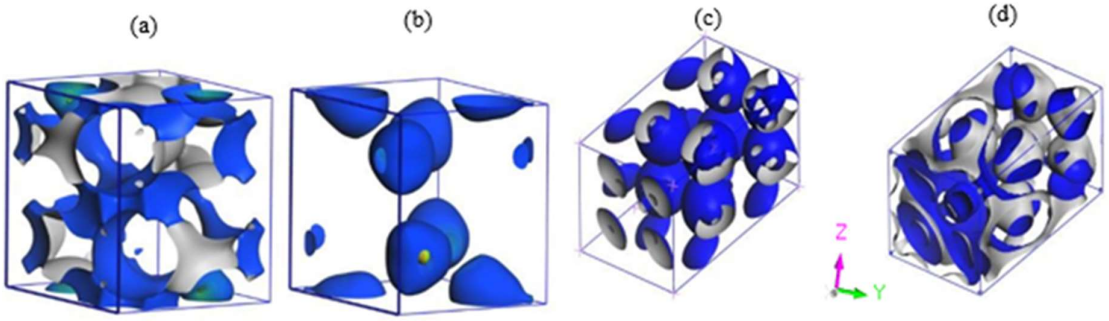

Fig. 10: Fermi surface of LiMnO4 (a), (b) and LiMn2O4 (c), (d) at zero temperature and pressure.

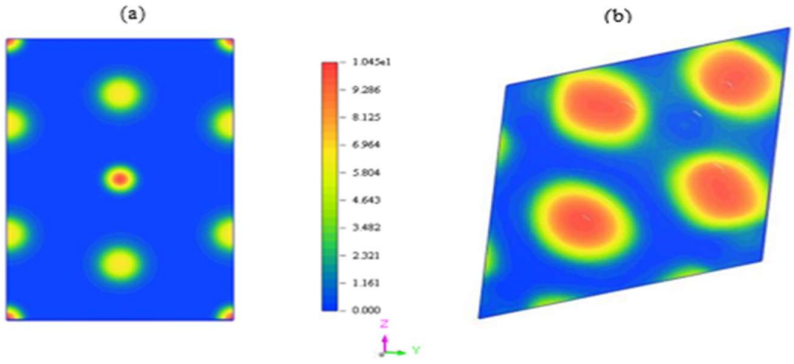

Fig. 11: The 2-D charge density of LiMnO4 and LiMn2O4 at zero temperature and pressure.

Fermi surface and Charge Density

The Fermi surface contour is obtained from the crystalline of its periodicity and symmetry of lattice and the occupied electronic energy bands of the solid. The occupied and unoccupied electron states which separates at zero temperature is formed in reciprocal space of the Fermi surface. The vibrational and dynamical properties of any electron on the surface widely depend on the position of an electron in the Fermi surface. Hence, the shape of the Fermi surface concerning the Brillouin zone is a guideline of the electrical, magnetic, optical, and thermal

properties of any materials [57 - 62]. The Fermi surface topologies of LiMnO4 and LiMn2O4 at zero pressure and zero temperature are shown in Figs.10 (a) to (d), respectively. The outer and inner shapes of the Fermi surfaces are complicated and quite different with each other in both cases. The electron-like pocket and hole-like pocket Fermi surfaces are existing for both compounds. To realize the distribution concentrations of the electron density of LiMnO4 and LiMn2O4, the valence electronic charge density maps (in the units of e/Å3) have been depicted in Figs. 11 (a) and (b), respectively. From the charge distributions it reveals that O atoms exhibit a strongly directional bonding compared to Li and Mn atoms. The atom which has large value of electronegativity (electric charge) attracts electron density towards itself [37]. As the electronegativity difference is large, the electric charge around O (3.44) atom is greater than around Mn (1.55) and Li (1.23) atoms. Also, the radius of the element is related with the charge negativity. The radius of Mn and Li is 1.39Å and 1.23 Å, respectively [63].

For LiMnO4 and LiMn2O4 both the cases there contain covalent and ionic bonds (O-Li-O, Li-Mn ionic bond, and Mn-Mn polar covalent bond). The localization of charge density around the core region of the O and Li is spherical due to ionic bonds. In the case of valence band area, there is a polar covalent bonding between Mn-Mn. There is also a covalent bond exist between the Li-Li and O-O atoms itself. The crystallographic electronic charge densities in all planes are showing its both the ionic and covalent bonds [64].

Optical Properties

The analysis of the optical functions of any solid helps us to give a better understanding of the electronic structure. The optical properties study in modern physics, is very much interesting because when electromagnetic radiation is incident on the materials, the materials respond in different way. The optical properties of LiMnO4 and LiMn2O4, can be derived from the comprehension of the complex dielectric function, ε(ω). Generally, there are two contributions, namely, intraband and interband transitions for ε(ω). However, the latter contributions are vital metals [65]. One can expressed the complex dielectric function as $\varepsilon(\omega) = \varepsilon_1(\omega) + i\varepsilon_2(\omega)$. Within the selection rules, the imaginary part ε2(ω) is obtained from the momentum matrix elements between the occupied and unoccupied wave functions. Using the Kramers–Kronig relation, the real part ε1(ω) of the dielectric function can be derived from the imaginary part. The comprehension study for both ε1(ω) and ε2(ω) permits to calculate the important optical constants such as the refractive index n(ω), extinction coefficient k(ω), conductivity, optical reflectivity R(ω), absorption coefficient α(ω), and energy-loss spectrum L(ω) using the expressions given in ref. [66]. The calculational approaches are well established and widely available in chapter four and hence not be repeated here. The estimated optical properties of LiMnO4 and LiMn2O4 at ground state are presented in Figs. 12 (a) to (h) for the photon energy range up to 50 eV for the polarization vector [100].

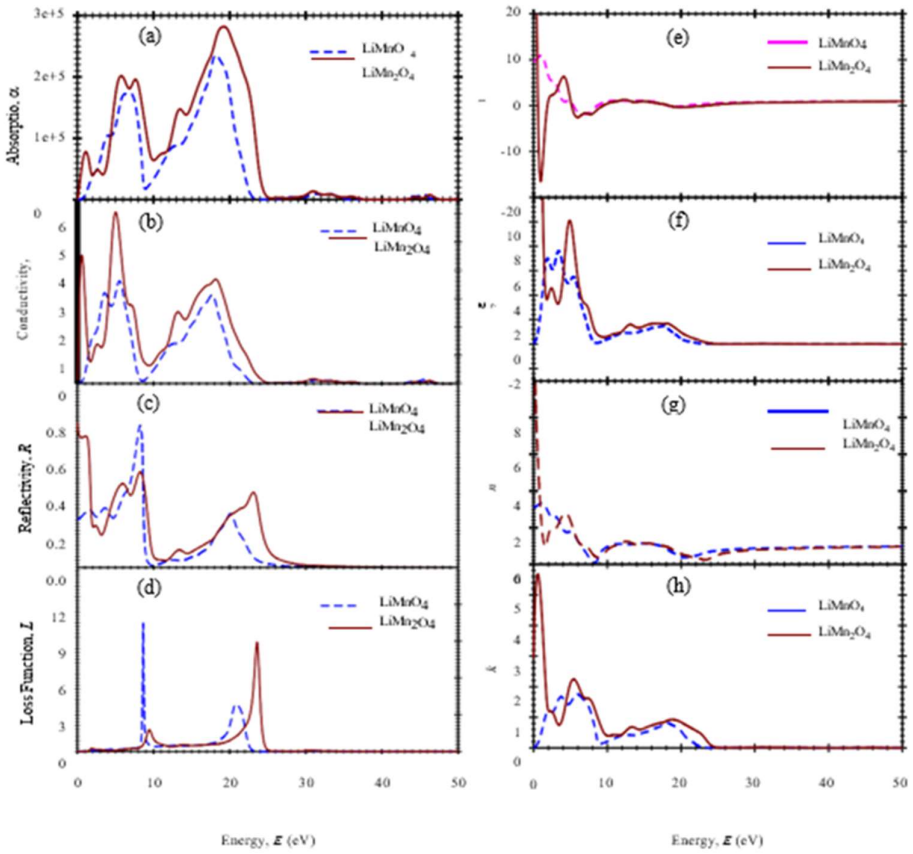

Fig.12: Absorption (a), Conductivity (b), Reflectivity (c), Loss function, Dielectric functions (e, f) and refractive indices (g, h) LiMnO4 for and LiMn2O4 respectively at ambient condition.

Fig. 12 (a) shows the absorption coefficient spectra of LiMnO4 and LiMn2O4, respectively, which begin above 0.0 eV photon energy for LiMnO4 due to their band gap existence. On the other hand, the absorption started from zero photon energy for LiMn2O4 which indicates there is no band gap existence. We observed that the absorption coefficient spectrum with one peak between 0.0 eV and 10.0 eV for both cases that rises and then sharply decreases at around 10.0 eV. But for both compounds, the absorption is highest at energy of about 20.0 eV. The absorption rate is higher for the LiMn2O4 comparing to the LiMnO4. The nearly same feature can be seen for both the materials under study from the energy range from above 25.0 eV.

The photoconductivity starts with the photon energy above zero for LiMnO4 whereas photoconductivity starts at zero photon energy for LiMn2O4 Fig. 12 (b). This result shows that there is no band gap for LiMn2O4. In contrasts, there is a band gap that is evident from band structure calculations also for LiMnO4. We observe that the maximum optical conductivity occurs at the energy of 6.0 eV for both cases. This implies that LiMn2O4 should be highly electrically conductive than LiMnO4 when the incident radiation has energy within this energy range. The photoconductivity reaches zero at about 25.0 eV LiMn2O4. In contrast at 22.5 eV the photoconductivity reaches zero for LiMnO4. There is no photoconductivity were observed for both the phases as the photon energy more than the 25.0 eV. We are not aware of any other

optical properties investigations through theoretical calculations or experimental data of LiMnO4 and LiMn2O4. Thus, for the further investigations, these results would provide a useful reference study. The calculated optical reflectivity R(ω) as a function of incident photon energy is displayed in Fig. 12 (c) with equilibrium conditions. It is observed from the figure that LiMnO4 has the maximum reflectivity (~80%) in the infrared region as well as in the ultraviolet region. Hence, we may conclude that LiMnO4 compound under study may be used as a coating to reduce the solar heating system.

The absorption and reflection are closely related with the loss function. The fast electron moving through the materials reveals the Loss function. The figure clearly shows that that at the time of electron traversing maximum reflectivity observes where the minimum absorption takes place. The electron energy loss function L(ω) is depicted in Fig. 12 (d) at equilibrium conditions. The peaks in L(ω) spectra represent the characteristic associated with the plasma resonance and the corresponding frequency is the so-called plasma frequency, ωP, which occurs at ε2< 1 and ε1 reaches the zero point [65-71]. The peaks of L(ω) is located at 8.5 eV and 9.5 eV to the corresponds of plasma frequency for LiMn2O4 and LiMnO4, respectively. When the incident light has a frequency higher than the plasma frequency of the solid, it will be transparent and will change the phases.

Dielectric function is the most general property of a solid, which modifies the incident electromagnetic wave of light. Fig. 12 (e, f) shows the real and imaginary parts of the dielectric function for LiMnO4 and LiMn2O4 for equilibrium and ambient pressure where band gap overlaps for LiMn2O4 and there is a band gap exist for LiMnO4. The electronic band structure analysis shows that LiMnO4 is non-metallic whereas LiMn2O4 shows metallic behaviour. Therefore, Drude term correction is required to include the effect of metallicity. For all calculations, we have used 0.5 eV Gaussian smearing. The real part ε1 goes through zero from below at about 16.5 and 2.5 and the imaginary part ε2 approaches zero from above at about 120.0 eV and 0.0 eV for LiMn2O4 and LiMnO4, respectively. Metallic reflectance characteristics are exhibited in the range $\varepsilon 1 < 0$. However, the range of both real and imaginary parts shifted to zero at an energy of 25.0 eV. The electromagnetic wave propagation of an through a solid is given by the frequency dependent complex refractive index N = n+ik, where the imaginary part k, the extinction coefficient and the real part n is related to the velocity is related to the decay or damping of the oscillation amplitude of the incident electric field.

The refractive index and extinction coefficient are illustrated in Figs. 12 (g, h) at equilibrium and ambient conditions. The static refractive index n (0) is found to have the maximum value at around 0.0 eV for the LiMn2O4 whereas for LiMnO4 it is found to be at an energy of 1.5 eV. The extinction coefficient, k shows the maximum value at 1.50 eV for LiMn2O4 whereas for LiMnO4 6.5 eV then it decreases rapidly and turns to zero at about 25.0 eV, 23.0 eV for LiMn2O4 and LiMnO4, respectively.

Thermodynamic Properties: Properties at Elevated Temperature and Pressure

The elastic parameters and analogous physical quantities like, internal energy, Debye temperature, entropy, etc. allow an extensive knowledge of the interrelation among the

mechanical properties of the solids and the electronic and phonon structure of materials. The thermodynamic properties of the LiMnO4 have been investigated by applying the quasi-harmonic Debye model, a detailed description of which can be found in the literature [72]. Here we computed the Bulk modulus, Specific heat capacities, and Volume thermal expansion coefficient at different temperatures and pressures. For this purpose, we have used E–V data which is obtained from the third-order Birch–Murnaghan equation of state [72-74] employing zero temperature and zero pressure equilibrium values, E0, V0, B0, based on the DFT calculations. The thermodynamic properties were calculated from 0 to 1000 K temperature and 0 to 70 GPa pressure range, where the quasi-harmonic Debye model remains valid.

Bulk Modulus

The temperature dependence of adiabatic bulk modulus, B for LiMnO4 and LiMn2O4 at P = 0 GPa is shown in Fig. 13 (a) and (b). Our calculations exhibit that, B0 value for LiMnO4 decreases rapidly for temperatures up to 1000 K in contrast Bs decreases slowly compared to the B0. Similar properties were observed for LiMn2O4 also. For B0 and Bs the values of LiMnO4 decreases by 26.77% and 12.12%, respectively. In contrast, the values for LiMn2O4 changes by 11.61% and 5.59%, respectively. Also, the variation of bulk modulus at 300 K, 600 K, and 900 K temperatures with pressure is shown in Fig. 13 (b). It is observed from the figure that the pressure dependences of bulk modulus increase at 523.03%, 477.57%, 441.37% and 421.01% with constant temperature 0 K, 300 K, 600 K and 900 K, respectively from 0 to 70 GPa. Almost the same properties were found for LiMn2O4 material also. The inset figure shows the clear variation with temperature and pressure.

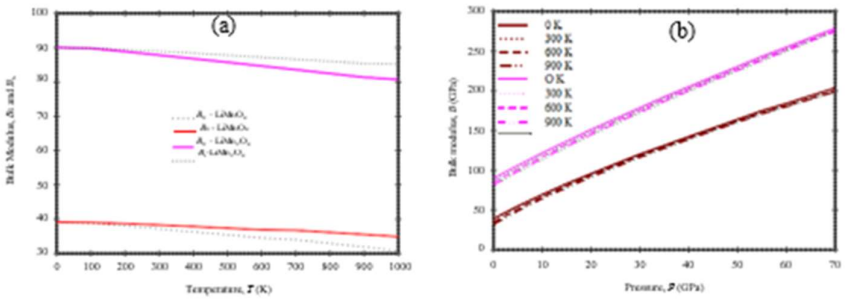

Fig. 13: Temperature (a) and pressure (b) dependent bulk modulus.

Specific Heat Capacities

Fig. 14 and 15 represent the estimated results on the temperature dependence of constant-pressure Cp, of LiMnO4. As the temperature increases, phonon thermal softening occurs and hence heat capacities increase. The difference between CP and CV for LiMnO4 due to the thermal expansion caused by anharmonicity effects [75] and also which can be explained by the relation between C_P and C_V as follows:

$$C_P - C_V = \alpha_V^2 (T) BVT$$

Where αV, B, V, and T are the volume thermal expansion coefficient, bulk modulus, volume and absolute temperature, respectively.

The specific heat exhibits the Debye T3power-law behavior at the low-temperature limit, and at temperature more than room temperature (T>300 K), the anharmonic effect is suppressed on heat capacity, and CV approaches the classical asymptotic limit C_V = 3nNkB = 144.0 J/mol.K and C_V = 3nNkB = 168.0 J/mol.K for LiMnO4 and LiMn2O4, respectively. These results exhibit the fact that at low temperature the interactions between ions in LiMnO4 have a large effect on heat capacities. The calculations of Fatmi et al [75] for a similar type of compound coincide with our results. To evaluate the electronic contribution to specific heat through the Sommerfeld constant, γ within the free electron model: γ= (1/3)π^2 〖πk〗 ^2 BN(EF), we can use N(EF) from the investigated DOS for the three alloys. The specific heat capacities are decreases with increasing pressure. It is observed that the Cp decreases at 300 K, 600 K, and 900 K are (43.75 %, 20.0%), (16.0%, 7%) and (14%, 6%) for LiMnO4 and LiMn2O4, respectively. It is clear that at a lower temperature, the change is higher.

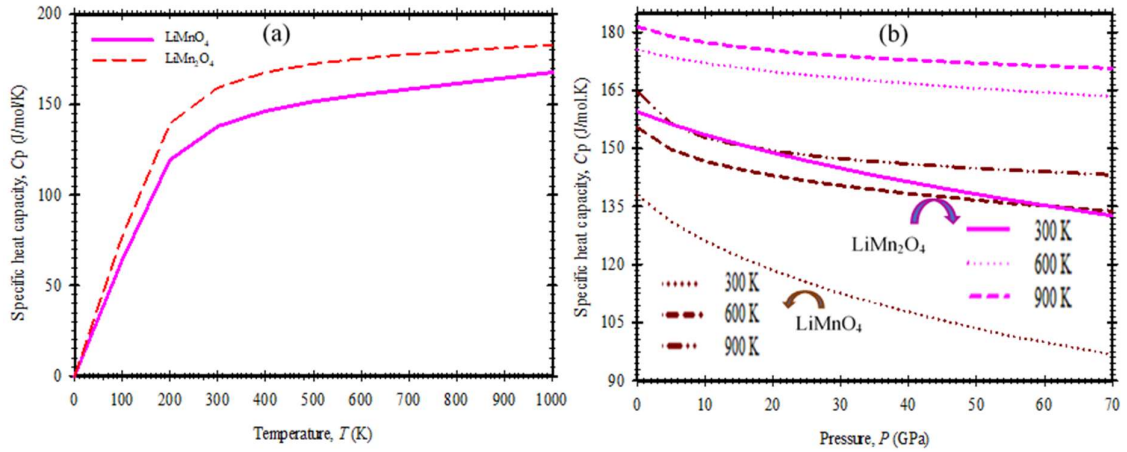

Fig. 14: Temperature (a) and Pressure (b) dependent specific heat capacity, Cp.

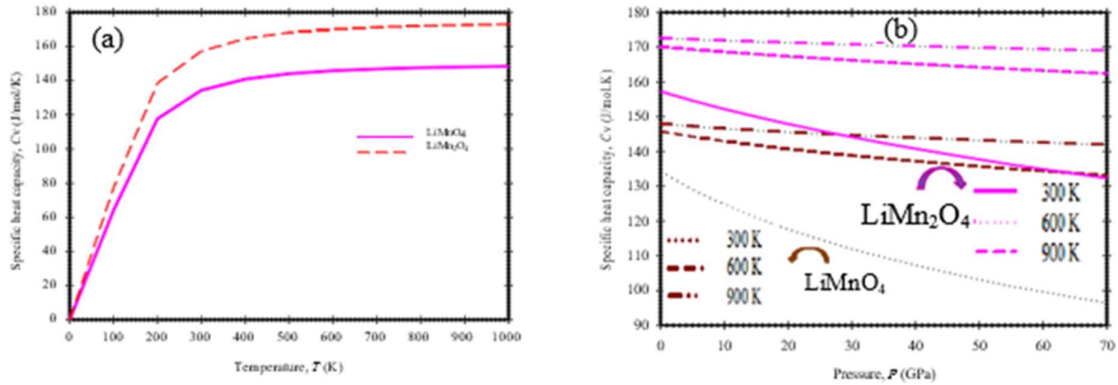

Fig. 15: Temperature (a) and pressure (b) dependent on specific heat capacity, Cv at different temperatures.

7.3 Thermal Expansion Co-efficient

The temperature dependence volume thermal expansion coefficient, α_V reflects at constant pressure: α = 1/V (dV/dT) . Fig.16 (a) depicts the temperature dependence of α_V at P = 0 GPa. The coefficient, α_V increases sharply as the temperature rises up to ~300 K and then gradually reaches a linear increase with enhanced temperature and the propensity of increment

goes to moderate state, which means that at high temperature α_V is very relatively very small. For a given temperature, the coefficient decreases exceedingly with the increase of pressure. The pressure dependence of α_V at different temperatures is presented in Fig.16 (b). The stronger the inter-atomic bonding, the smaller is the thermal expansion. The value of α_V are found to be 7.93×10^(-5) K^(-1) for LiMnO4 and 3.63 ×10^(-5) K^(-1) for LiMn2O4 at P = 0 GPa at T = 1000 K. For a given temperature, the coefficient α_V sharply decreases with the increase of pressure. At low temperatures, the value of thermal expansion co-efficient varies very sharply whereas, at the high temperature, it decreases very slowly. The higher value of LiMnO4 indicates that it is softer compared to LiMn2O4. Up to now, there are no experimental or other theoretical investigations are found for the thermal properties of LiMnO4. Our investigations may serve as a guide for future works. Another fact is that the change is lower for LiMn2O4 compared to LiMnO4.

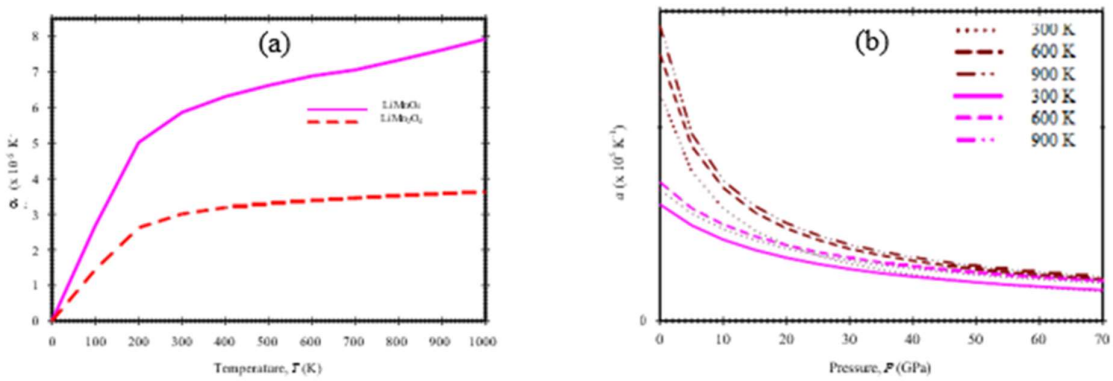

Fig. 16: Temperature (a) and pressure (b) dependent thermal expansion coefficient, α.

Conclusion

The observed equilibrium lattice parameters of LiMnO4 and LiMn2O4 are found to be in excellent agreement with available theoretical and experimental results. The independent elastic constants (Cij) satisfy the Born stability criteria, indicating the mechanical stability of LiMnO4 and LiMn2O4. In the case of tensor analysis, a common thing is present for LiMnO4 and LiMn2O4; all the elastic moduli are to be anisotropic. In contrasts, the linear compressibility of LiMn2O4 was found to be isotropic. At the equilibrium condition, there exists a band gap (0.852) for LiMnO4. On the other hand, there was a band overlap for LiMn2O4. The characteristic pseudogap around the Fermi level shows the presence of directional covalent bonding. From electronic charge densities map both ionic and covalent bonds in nature were observed in all crystallographic planes. The reflectivity is high (~80%) in the IR-visible-UV region was observed for LiMnO4, showing that this material can be considered as a possible coating material to avoid solar heating. The specific heat exhibits the Debye T3power-law behavior at low temperature range and at high temperature (T>300 K), the anharmonic effect is suppressed on heat capacities. The higher value of LiMnO4 specifies that it is softer compared to LiMn2O4.

References

[1]. P.G. Bruce, B. Scrosati, and J.-M. Tarascon, Angewandte Chemie International Edition 47, 2930 (2008). [2]. Y.-G. Guo, J.-S. Hu, and L.-J. Wan, Advanced Materials 20, 2878–2887 (2008).
[3]. F. Cheng, J. Liang, Z. Tao and J. Chen, Advanced Materials 23, 1695 (2011).
[4]. D. Chen, X. Mei, G. Ji, et al., Angewandte Chemie International Edition 51, (2012) 2409.
[5]. V. Etacheri, R.Marom, R.Elazari, G.Salitra, D.Aurbach, Energy & Environmental Science 4, 3243 (2011). [6]. M. S. Whittingham, Chemical Reviews 104, 4271 (2004).
[7]. M.-K. Song, S. Park, F.M. Alamgir, et al., Materials Science and Engineering Reports 72, 203 (2011). [8]. H. Xia, Y.S. Meng, M.O. Lai, and L. Lu, Journal of The Electrochemical Society 157, A 348 (2010). [9]. H. Xia, L. Lu, and Y. S. Meng, Applied Physics Letters 92, 011912 (2008).
[10]. A. Manthiram, The Journal of Physical Chemistry Letters 2, 176 (2011).
[11]. R. Pitchai, V. Thavasi, S.G. Mhaisalkar, et al. Journal of Materials Chemistry 21, 11040 (2011).
[12]. T. J. Patey, R. Buchel, M. Nakayama, and P. Novak, Physical Chemistry Chemical Physics 11, 3756 (2009). [13]. Y. Yang, C. Xie, R. Ruffo, et al. Nano Letters 9, 4109 (2009).
[14]. E. Hosono, T. Kudo, I. Honma, et al, Nano Letters 9, 1045 (2009).
[15]. Y. k. Zhou, C. M. Shen, J. Huang, et al. Materials Science and Engineering B 95, 77 (2002). [16]. Y. -L. Ding, J. Xie, G. -S. Cao, et al. Advanced Functional Materials 21, 348 (2011).
[17]. X. Li, F. Cheng, B. Guo, et. al. The Journal of Physical Chemistry B 109, 14017 (2005).
[18]. T. J. Patey, R. B¨ uchel, S. H. Ng, et al. Journal of Power Sources 189, 149 (2009). [19]. H. Xia, K. R. Ragavendran, J. Xie, et al. Journal of Power Sources 212, 28 (2012).
[20]. J. Fvon B. ulow, H.-L.Zhang, et al. Advanced Energy Materials 2, 309 (2012).
[21]. S. Y. Han, I. Y. Kim, K. Y. Jo, et. al. The Journal of Physical Chemistry C 116, 7269 (2012).
[22]. H. Xiaa, Z. Luob, and J. Xie, Progress in Natural Science: Materials International 22(6), 572 (2012). [23]. J. P. Perdew, K. Burke and M. Ernzerhof,Phys. Rev. Lett.77, 3865 (1996).
[24]. P. Hohenberg and W. Kohn,Phys. Rev. B136, 864 (1964). [25]. W. Kohn and L. J. Sham,Phys. Rev. A140, 1133 (1965).
[26]. S. J. Clarket al.,Zeitschrift f r Kristallographie 220, 567 (2005).
[27]. D. Vanderbilt,Phys. Rev. B41, 7892 (1990).
[28]. T. H. Fischer and J. Almlof,J. Phys. Chem. 96, 9768 (1992). [29]. H. J. Monkhorst and J. D. Pack,Phys. Rev. B13, 5188 (1976).
[30]. F. D. Murnaghan,Finite Deformation of an Elastic Solid (Wiley, New York, 1951). [31]. M. A. Blanco, E. Francisco and V. Lua ñ a,Comput. Phys. Commun.158, 57 (2004). [32]. F. Birch,J. Geophys. Res. 83, 1257 (1978).
[33]. Z. Sunet al.,Appl. Phys. Lett. 83, 899 (2003).
[34]. J. M. Schneider et al., Solid State Commun.130, 445 (2004). [35]. M. Khazaeiet al.,Sci. Technol. Adv. Mater.15, 014208 (2014).
[36].D. Fischer, R. Hoppe, W. Schaefer,K. S. Knight, K.S, Li (Mn O4)", Zeitschrift fuer Anorganische und Allgemeine Chemie, 619, 1419-1425 (1993).
[37]. https://materialsproject.org/materials/mp-19438/

[38]. M.M. Thackeray, A. de Kock, M.H. Rossouw, D. Liles, R. Bittihn, and D. Hoge, J. Electrochem. Soc., 139 (2) 363 (1992).
[39]. M. M. Thackeray, P. J. Johnson, L.A. de Picciotto, et al. Mat. Res. Bull., 19, 179 (1984).
[40]. M.N. Richard, I. Keotschau, and J.R. Dahn, J. Electrochem. Soc., 144, 55 (1997).
[41]. X. Q. Yang, X. Sun, S.J. Lee, J. McBreen, et al. Electrochem. Solid St. Lett., 2, 157 (1999). [42]. S.-H. Kang, J.B. Goodenough, and L.K. Rabenberg, Chem. Mater., 13, 1758 (2001).
[43]. F. Mouhat and F.-X. Couder, Phys. Rev. B 90, 224104 (2014).
[44]. R. Hill and F. Milstein, Phys. Rev. B 15, 3087 (1977).
[45]. F. Milstein, R. Hill, and K. Huang, Phys. Rev. B 21, 4282 (1980).
[46]. Wolfram Research, Inc., Mathematica, Version 10.0.1, Champaign, IL (2014).
[47]. A. Marmier, ZA Lethbridge, RI. Walton, et al. Comput. Phys. Commun.181, 2102 (2010).
[48]. A. U. Ortiz, A. Boutin, AH. Fuchs et al. Phys. Rev. Lett., 109, 195502 (2012).
[49]. J. C. Tan , B. Civalleri, CC. Lin, et al. Phys. Rev. Lett., 108, 095502 (2012). [50]. A. U. Ortiz , A. Boutin, AH. Fuchs, et al. J. Chem. Phys.138, 174703 (2013). [51]. M. M. Ali and S. H. Naqib, RSC Adv., 10, 31535 (2020).
[52]. M. Guinan, D. Steinberg, Journal of Physics and Chemistry of Solids. 35 (11), 1501 (1974).
[53]. L. D. Landau, L. P. Pitaevskii, A. M. Kosevich, et al. Theory of Elasticity, vol. 7. (Theoretical Physics). 3rd Ed. Pergamon: Oxford. (1970).
[54]. H. M. Ledbetter and A. Migliori, J. Appl. Phys. 100, 063516 (2006). [55]. W. C. Hu, Y. Liu, D. J. Li, et. al. Comput. Mater. Sci. 83, 27 (2014).
[56]. W. C. Hu, Y. Liu, D. J. Li, et al. Physica B 427, 85 (2015).
[57]. J. Zhu, Y. Wang, S. Li, et. al. Inorg. Chem. 55, 5993 (2016). [58]. S. B. Dugdale, Physica Scripta. 91 (5), 053009 (2016).
[59]. N. Ashcroft, and N. M. Mermin, Solid-State Physics (New edition - 2021).
[60]. W. A. Harrison, Stanford University, DOVER Publications, Inc., New York 1989.
[61]. T.-S. Choy, J. Naset, J. Chen, S. Hershfield, and C. Stanton. A database of fermi surface in virtual reality modeling language (vrml). Bulletin of The American Physical Society, 45 (1), L36 (2000).
[62]. J. M. Ziman, Electrons in Metals: A short Guide to the Fermi Surface. London: Taylor & Francis (1963).
[63]. J. M. Ziman, Contemp. Phys. 3, 321 (1962).
[64]. IUPAC, Compendium of Chemical Technology, 2nd edn. (the “Gold Book”) (1997). Online corrected version: (2006) “Electronegativity”.
[65]. W. B. Jensen, Journal of Chemical Education 73, (1996)11.
[66]. A. H. Reshak, V. V. Atuchin, S. Auluck and I. V. Kityk, J. Phys. Condens. Matter. 20, 325234 (2008). [67]. M. Fatmi, M. A. Ghebouli, B. Ghebouli, et al. Journ. Phys. 56, 935 (2011).
[68]. S. Li, R. Ahuja, M. W. Barsoum, et. al. Appl. Phys. Lett. 92, 221907 (2008).
[69]. R. Saniz, L. H. Ye, T. Shishidou, A. J. Freeman, J. Phys. Rev. B 74, 014209 (2006). [70]. M. Fox, Optical Properties of Solids, Academic Press, New York 1972.
[71]. J. S. De Almeida and R.Ahuja, Phys. Rev. B 73, 165102 (2006).
[72]. M. A. Blanco, E. Francisco, and V. Luan˜ a, Comput. Phys. Commun. 158, (2004) 57.
[73]. F. Birch, J. Geophys. Res. 83, 1257 (1978).

[74]. M. S. Ali, A. K. M. A. Islam, M. M. Hossain, et al. Physica B 407, 4221 (2012).
[75]. M. Fatmi, M. A. Ghebouli, B. Ghebouli,T. Chihi, S. Boucetta,, Z. K. HeibaRom. Journ. Phys. 56, 935 (2011).